High resolution full-field optical coherence tomography microscope for the evaluation of freshly excised skin specimens during Mohs surgery: A feasibility study

Manu Jain (✉ jainm@mskcc.org)
Memorial Sloan Kettering Cancer Center

Shu-Wen Chang
National Taiwan University Hospital

Kiran Singh
Memorial Sloan Kettering Cancer Center

Nicholas R. Kurtansky
Memorial Sloan Kettering Cancer Center

Sheng-Lung Huang
National Taiwan University Hospital

Homer H. Chen
National Taiwan University Hospital

Chih-Shan Jason Chen
National Taiwan University Hospital

Abstract

Histopathology for tumor margin assessment is time-consuming and expensive. High-resolution full-field optical coherence tomography (FF-OCT) images fresh tissues rapidly at cellular resolution and potentially facilitates evaluation. Here, we define FF-OCT features of normal and neoplastic skin lesions in fresh ex vivo tissues and assess its diagnostic accuracy for malignancies. For this, normal and neoplastic tissues were obtained from Mohs surgery, imaged using FF-OCT, and their features were described. Two expert OCT readers conducted a blinded analysis to evaluate their diagnostic accuracies, using histopathology as the ground truth. A convolutional neural network was built to distinguish and outline normal structures and tumors. Of the 113 tissues imaged, 95 (84%) had a tumor (75 BCCs and 17 SCCs). The average reader diagnostic accuracy was 88.1%, with, a sensitivity of 93.7%, and a specificity of 58.3%. The AI model achieved a diagnostic accuracy of 87.6%±5.9%, sensitivity of 93.2%±2.1%, and specificity of 81.2%±9.2%. A mean intersection-over-union of 60.3%±10.1% was achieved when delineating the nodular BCC from normal structures. Limitation of the study was the small sample size for all tumors, especially SCCs. However, based on our preliminary results, we envision FF-OCT to rapidly image fresh tissues, facilitating surgical margin assessment. AI algorithms can aid in automated tumor detection, enabling widespread adoption of this technique.

Introduction

Non-melanocytic skin cancer (NMSC) is the most prevalent cancer worldwide, accounting for ~ 5.4 million cases diagnosed and treated annually in the US alone[1]. Among all NMSCs, basal cell carcinoma (BCC) is the most common type (~ 4.3 million cases), followed by squamous cell carcinoma (SCC; ~1 million cases)[1]. NMSCs are rarely fatal and seldom metastatic, but they can be highly infiltrative and aggressive and have a high recurrence rate[2].

Surgical excision and Mohs micrographic surgery are widely accepted procedures for the margin assessment and complete removal of the NMSC with a high cure rate of 95−99% respectively[3]. To achieve a high cure rate and preserve healthy skin, histopathological examination of the excised tissue is the gold standard. However, histopathology evaluations require time-consuming tissue preparation, extensive laboratory facilities, and well-trained technicians[4,5].

Ex vivo optical imaging devices including confocal microscopes and optical coherence tomography (OCT) have been developed for the rapid evaluation of fresh tissues to obviate tissue processing[5−11]. In this article, we describe the utility of a novel full-field OCT (FF-OCT) microscope (ApolloVue® B100 image system, Apollo Medical Optics, Ltd.) device. OCT relies on a low coherence interferometer and the light scattering properties of skin structures to construct cross-sectional images of tissue[12]. However, the existing OCT devices have a low resolution (3−10 μm axial and 3-7.5 μm lateral resolution), which hinders the differentiation of normal skin structures from tumors and tumor subtyping[12,13]. In contrast, the novel FF-OCT microscope has an axial resolution of 1.5 μm and a lateral resolution of 1.1 μm, which is far superior to the existing OCT devices. Wang et al demonstrated that even a novice (without OCT experience) can read these images with 93−100% sensitivity and 21−54% specificity. However, this study was performed on paraffin-embedded thick tissue sections, which doesn't equate to the evaluation of freshly excised tissues[14].

Although the emergent cellular-resolution optical coherence tomography (OCT) could significantly accelerate the clinical adoption of OCT to assist physicians in interpreting images[15−18], interpretation of OCT images often requires an expert with extensive training in reading these images, posing a major barrier to integrating OCT in clinics[6,9]. Thus, deep learning algorithms, in particular convolutional networks (CNN), have become a powerful tool for analyzing medical images to assist physicians in detecting, classifying, segmenting, and even diagnosing tissue images[19]. CNN has the advantage of automatically extracting features and is not limited to features defined by the human eye. At present, many studies have used CNN to identify basal cell carcinoma in stained images[20] and segment nuclei from stained images[21,22] and dermal fillers in OCT images of mouse skin[23].

In our study, for the first time, we imaged fresh, non-labeled (without using any exogenous dye/contrast agent) tissues obtained during Mohs surgery using a high-resolution FF-OCT microscope. First, we defined FF-OCT features of all normal skin structures

and various NMSC tumors, particularly BCC, and some benign lesions. Next, to demonstrate the feasibility of this device in a surgical setting, we performed a blinded analysis by two OCT experts (1 pathologist and 1 Mohs surgeon) to access the diagnostic accuracy (sensitivity and specificity) of detecting tumors. Lastly, to overcome the limitations of reading gray-scale images and mitigate the mosaic artifacts due to image stitching, we generated a deep-learning algorithm that can differentiate BCC tumor nodules from sebaceous glands and other non-tumor tissues.

Material And Methods

Patient cohort, consenting, and tissue collection: This study was conducted at Memorial Sloan Kettering Skin Cancer Center, Hauppauge, New York between April 2017 and February 2020. Patients undergoing Mohs surgery for NMSCs consented to an institutional review board-approved protocol (# 08 – 006) for the collection of fresh discarded specimens (cut tangentially) after the completion of pathology analysis. Our collection did not compromise Mohs procedures or patient care. We excluded patients younger than 18 years of age. Also, large samples that exceeded the imaging window area (20x20 mm) of the tissue holder or tissues thinner than 1 mm were not included in the study.

Tissue preparation and FF-OCT imaging: Discarded tissues were thawed from the frozen blocks and rinsed in normal saline. They were then placed in the plastic cassette (provided with the device) with the frozen section cut surface facing the glass window for imaging. Nicks and their associated color codes were applied on the edges of the specimens for the purpose of tissue orientation and subsequent histopathology correlation. A drop of glycerin was applied to the glass window before the tissue placement. The cassette was then closed with a cover to secure the specimen in place. The tissue flattening was achieved using the sponge cushion lining the inner surface of the cover. A drop of mineral oil was added to the lens and the cassette was then inserted into the imaging well of the device for scanning. The technological details of the device have been previously described[14]. Once the scanning process was completed, the entire plane of 10 to 30 microns below the cut surface of the specimen was visualized as one mosaic composed of multiple small fields of view (FOV; 800 μm x 600 μm). The scanned images were stored on a connected computer for analysis[14].

Blinded analysis: The two expert readers (MJ, a pathologist; and CSJC, a Mohs surgeon), first trained themselves by studying 10 mosaics from BCC tumors and defined FF-OCT features for BCC and surrounding normal structures (epidermis, hair follicles, sebaceous glands, eccrine ducts, adipose tissue, vessels, and nerves), comparing them with their corresponding histopathology. Later a test set was created using 113 FF-OCT mosaics (from 113 fresh tissues). The images used for training were removed from the test set. All the FF-OCT images collected were de-identified and were assigned a study number and provided to the experts for reading independently. The readers were blinded to the histopathology diagnosis. Each of the readers recorded findings including the presence or absence of the tumor, type, and subtype of tumor in a spreadsheet. Clinical data was also collected for the consented patients including name, age, gender, clinical diagnosis, and location of the lesion. Corresponding histopathology sections (created at the time of Mohs evaluation) provided the closest mirror images of the FF-OCT mosaics and were used as ground truth for the concordance of FF-OCT reading.

Deep-learning algorithm: For the artificial intelligence (AI) algorithm, images from 23 nodular BCC (nBCC) were used. The image sizes were variable, and each image had more than 5,000 x 5,000 pixels with a pixel separation of 1.332 μm. The images were chopped into patches with 512 x 512 pixels to accommodate the limitations of computation power and storage capacity.

A convolutional neural network (CNN) classification model was built on top of the U-Net with symmetric down and up samplings result for nBCC detection[17,24,25] (Fig. 1). During the CNN training phase, 1,253 image patches with nBCC were used. The largest receptive field is 186 x 186 μm^2. During training, the cross-entropy loss was used as the baseline for evaluation with 5-fold cross-validation. In addition to mitigation of imbalanced nBCC and non-nBCC classes, the focal loss was also adopted to improve the segmentation performance. As shown in Eq. (1), the focal loss is defined to down-weight easy examples and focus training on hard negatives. The focal loss down weights easy examples with a factor of (1 – pt)γ so that the model can focus on learning the misclassified pixels[24].

$$\mathrm{FL}\left(\mathrm{p_t}\right) = -\alpha_t(1-\mathrm{p_t})^\gamma \log\left(\mathrm{p_t}\right)$$

1

where α_t is the weighting factor to address the class imbalance issue, γ is the focusing parameter, and p_t is defined in Eq. (2)].

$$p_t = \begin{cases} p, if\, y = 1 \\ 1 - p, otherwise \end{cases}$$

2

where p ∈ [0,1], is the model's estimated probability for the class with y = 1 (nBCC pixels). In our two-class scenario, y= -1 for non-nBCC pixel.

The focal loss was first employed to eliminate the OCT mosaic artifacts. After the segmentation model, a classification model was used to differentiate the BCC tumor nodules from other tissues.

To quantitatively evaluate the image segmentation performance, mean intersection over union

(mIOU) was used to measure the overlapping between the predicted and annotated image pixels.

In addition to image segmentation, a classification model was built on top of the U-Net result for nBCC detection of the excised tissues. The post-segmentation image erosion process was applied to

reduce the fragmented dusty pixels. In addition, a voting strategy was adopted on the outputs of the U-Net patches by partitioning each of the 512x512-pixel patches to 128x128-pixel patches for both hard and soft votings. As a result, 22,386 small patches were generated for training, and among them, 10,193 small patches have nBCC pixels. Resnet18 was used as the classification model. And 5-fold cross-validation was applied.

Results

Patient demographics and lesion site: Hundred and ten patients were enrolled in this study. The male: female ratio was 1:4 and the average age of the patients was 63 years old (ranged 33 yo- 93 yo). Majority of the lesions 54/113 (47.8%) were located in the T-zone region (ear, eye, nose, lip, and chin), followed by 39/113 (34.5%) in the head and neck region (scalp, forehead, cheek, and neck), 14/113 (12.4%) on the extremities (arms, legs, hands, and feet), and only 6/113 (5.3%) on trunk and genitalia.

Histopathology diagnosis of the tissue samples collected (Table 1). A total of 113 tissues were collected and imaged with the FF-OCT device. Of which, 95 (84%) were positive for tumor including 73 (65%) BCCs, 15 (13%) SCCs, 2 basosquamous cell carcinoma (2%), and 5 others (4%). The most common BCC sub-type was the nBCC 46 (41%), followed by 43 (38%) infiltrative BCC (iBCC) or micro-nodular BCC (mnBCC) and the least common subtype was superficial BCCs (sBCC) 3 (3%). The rest 18/113 tissues (15.9%) were negative for tumors.

Table 1
Ground truth characteristics of the sample

Characteristic	N	%
Total	113	100%
Tumor Presence	95	84%
Tumor Type[1]		
BCC	73	65%
SCC	15	13%
BCC & SCC	2	2%
Other	5	4%
BCC subtypes[2]		
sBCC	3	3%
nBCC	46	41%
iBCC/mnBCC	43	38%
No BCC	38	34%

FF-OCT features of normal skin structures and tumors:

1) *Normal skin structures*: On a low magnification view, all skin layers including epidermis, dermis, and subcutis could be identified (Fig. 2). On a zooming-in, cellular details of each layer became evident. The epidermis appeared as a grayish linear stratified layer composed of multiple cells with a small dark nucleus and grayish cytoplasm. However, due to the difficulties in flattening the tissue edge completely on the imaging window, the epidermis could not be visualized in most of the tissues.

Hair follicles (Fig. 3) appeared as tubular to round structures with a central dark hole lined by an inner grayish epidermal layer and an outer bright fibrous layer. Sometimes a bright hair shaft was identified in the center of these follicles making their identification easy. Sebaceous glands (Fig. 3) appeared as round to oval varied-sized darkish (hypo-reflective) structures composed of multiple lobules separated by thin bright (hyper-reflective) fibrous septa. Due to their round shape, these glands were difficult to distinguish from nBCC; however, the presence of multiple small bright punctate particles, which we speculate to be the sebum particulates, aided in the distinction. Eccrine glands (Fig. 3) appeared as tightly packed clusters of small, round to oval grayish (hypo-reflective) structures separated by thin bright septa. Within the gland's lumen, small punctate bright particles (similar to sebaceous glands) could be seen. Eccrine ducts (Fig. 3) were seen within the clusters of eccrine glands as small roundish structures with a central dark (areflective lumen) and lined by grayish cells. The eccrine unit (glands and ducts) could be identified as embedded within dark (areflective) adipose tissue.

Smooth muscles (Fig. 4) could be identified as bundles of grayish (hypo-reflective) structures with intervening bright thin fibrous bands. Cigar-shaped dark elongated nuclei were seen within the muscle fibers. The smooth muscle bundles were seen lining the dark lumen of medium-sized blood vessels and attached to a hair follicle (as arrector pili muscle).

2) *Basal cell carcinoma*: Classic features of BCC could be identified on FF-OCT. BCC tumor nodules appeared as round to oval varied size structures composed of clusters of grayish (hyporeflective) pleomorphic cells with dark nuclei (Fig. 5, 6). These tumor nuclei were seen arranged perpendicular at the periphery of the nodule forming "palisading". Clefting was identified as a dark (areflective area) around tumor nodules.

In sBCC the tumor nodules were seen attached to the epidermis (Fig. 6a). In nBCC (Fig. 5) and mnBCC (Fig. 6b), the nodules were identified within the bright dermis. Palisading and clefting were prominent in both nBCC and mnBCCs. Necrosis was seen

in the bigger tumor nodules of nBCC as dissociated cells with some scattered bright particles within. The collagen appeared as bright (hyper-reflective) parallel bundles around the tumor nodules. iBCC had a distinct appearance (Fig. 6c). The tumor foci appear as darkish irregular strands (varied size and shape) composed of grayish clusters of cells with intervening bright strands of fibrous tissue. It was easier to identify these strands when they were clustered. Isolated foci were not readily detected. Additionally, in the area of iBCC, there was a complete loss of normal skin structures.

3) *Squamous cell carcinoma*: SCC was seen as sheets of polygonal cells with abundant grayish cytoplasm and enlarged irregular dark nuclei. Within the nucleus, a bright dot was often identified, which could be the nucleolus (Fig. 7).

4) *Other tumors*: Cylindroma (Fig. 8) appeared as well circumscribed large multi-lobated grayish structure within the dermis. Some of the lobules were surrounded by a bright thickened band of collagen. Each lobule is composed of monomorphic cells with a dark round nucleus and a rim of scant grayish cytoplasm. No clefting around the nodule was seen.

Blinded analysis:

Diagnostic accuracy of FF-OCT device in detecting residual tumors in the surgically excised fresh tissue

Readers 1 (CSJC) and 2 (MJ) each demonstrated high sensitivity (91.6% and 95.8%) and moderate specificity (55.6% and 61.1%), respectively, for detecting the presence of any malignant tumor in the margin (Table 2).

Table 2. Classification accuracies of two expert readers for detecting tumors in the surgically excised fresh tissue.

Assessment		Reader	Sensitivity (95% CI)		Specificity (95% CI)		Positive Predictive Value		Negative Predictive Value	
Tumor Presence		Average	93.7%		58.3%		92.2%		64.4%	
		Reader 1	91.6%	(84.1%, 96.3%)	55.6%	(30.8%, 78.5%)	91.6%	(84.1%, 96.3%)	55.6%	(30.8%, 78.5%)
		Reader 2	95.8%	(89.6%, 98.8%)	61.1%	(35.7%, 82.7%)	92.9%	(85.8%, 97.1%)	73.3%	(44.9%, 92.2%)
Tumor Classification	BCC	Average	87.3%		57.9%		80.4%		69.8%	
		Reader 1	85.3%	(75.3%, 92.4%)	52.6%	(35.8%, 69%)	78.1%	(67.5%, 86.4%)	64.5%	(45.4%, 80.8%)
		Reader 2	89.3%	(80.1%, 95.3%)	63.2%	(46%, 78.2%)	82.7%	(72.7%, 90.2%)	75.0%	(56.6%, 88.5%)
	SCC	Average	41.2%		95.8%		63.6%		90.2%	
		Reader 1	41.2%	(18.4%, 67.1%)	95.8%	(89.7%, 98.9%)	63.6%	(30.8%, 89.1%)	90.2%	(82.7%, 95.2%)
		Reader 2	41.2%	(18.4%, 67.1%)	95.8%	(89.7%, 98.9%)	63.6%	(30.8%, 89.1%)	90.2%	(82.7%, 95.2%)
	Other tumors	Average	30.0%		97.7%		41.7%		96.8%	
		Reader 1	20.0%	(0.5%, 71.6%)	99.1%	(95%, 100%)	50.0%	(1.3%, 98.7%)	96.4%	(91%, 99%)
		Reader 2	40.0%	(5.3%, 85.3%)	96.3%	(90.8%, 99%)	33.3%	(4.3%, 77.7%)	97.2%	(92%, 99.4%)
BCC Subtyping	sBCC	Average	0.0%		98.6%		NaN		97.3%	
		Reader 1	0.0%	(0%, 70.8%)	97.3%	(92.2%, 99.4%)	0.0%	(0%, 70.8%)	97.3%	(92.2%, 99.4%)
		Reader 2	0.0%	(0%, 70.8%)	100.0%	(96.7%, 100%)	NaN	(0%, 100%)	97.3%	(92.4%, 99.5%)
	nBCC	Average	79.3%		60.4%		57.9%		81.2%	
		Reader 1	73.9%	(58.9%, 85.7%)	59.7%	(47%, 71.5%)	55.7%	(42.4%, 68.5%)	76.9%	(63.2%, 87.5%)
		Reader 2	84.8%	(71.1%, 93.7%)	61.2%	(48.5%, 72.9%)	60.0%	(47.1%, 72%)	85.4%	(72.2%, 93.9%)
	iBCC/mnBCC	Average	33.7%		87.9%		62.1%		68.4%	
		Reader 1	25.6%	(13.5%, 41.2%)	87.1%	(77%, 94%)	55.0%	(31.5%, 76.9%)	65.6%	(55%, 75.1%)
		Reader 2	41.9%	(27%, 57.9%)	88.6%	(78.7%, 94.9%)	69.2%	(48.2%, 85.7%)	71.3%	(60.6%, 80.5%)
	No BCC	Average	56.6%		86.7%		68.1%		79.8%	

Abbreviations: CI: Confidence interval, BCC: Basal cell carcinoma, SCC: Squamous cell carcinoma, sBCC: Superficial basal cell carcinoma, nBCC: Nodular basal cell carcinoma, iBCC: Infiltrative basal cell carcinoma, mnBCC: micronodular basal cell carcinoma.

A fair degree of agreement was shown on this task, with a Cohen's Kappa = 0.327 **(Table 3)**. Readers were less accurate in differentiating SCC from BCC; each reader indicated the presence of SCC in 7 of 17 specimens containing a histologic SCC component. In addition, raters overcalled the presence of nodular BCC; they indicated the presence of this subtype in 54% and 58% of all cases and in those instances were correct 55.7% and 60.0% of the time (positive predictive values).

Assessment	Reader	Sensitivity (95% CI)		Specificity (95% CI)		Positive Predictive Value		Negative Predictive Value	
	Reader 1	50.0%	(33.4%, 66.6%)	84.0%	(73.7%, 91.5%)	61.3%	(42.2%, 78.2%)	76.8%	(66.2%, 85.4%)
	Reader 2	63.2%	(46%, 78.2%)	89.3%	(80.1%, 95.3%)	75.0%	(56.6%, 88.5%)	82.7%	(72.7%, 90.2%)

Abbreviations: CI: Confidence interval, BCC: Basal cell carcinoma, SCC: Squamous cell carcinoma, sBCC: Superficial basal cell carcinoma, nBCC: Nodular basal cell carcinoma, iBCC: Infiltrative basal cell carcinoma, mnBCC: micronodular basal cell carcinoma.

A fair degree of agreement was shown on this task, with a Cohen's Kappa = 0.327 (Table 3). Readers were less accurate in differentiating SCC from BCC; each reader indicated the presence of SCC in 7 of 17 specimens containing a histologic SCC component. In addition, raters overcalled the presence of nodular BCC; they indicated the presence of this subtype in 54% and 58% of all cases and in those instances were correct 55.7% and 60.0% of the time (positive predictive values).

Table 3
Agreement between two raters.

Assessment	Cohen's Kappa (95% CI)	
Tumor Presence	0.327	(0.092, 0.562)
Tumor Type	0.349	(0.184, 0.514)
BCC	0.362	(0.173, 0.551)
SCC	0.396	(0.119, 0.673)
Other	0.230	(-0.167, 0.626)
BCC subtypes		
sBCC	0.000	(-0.001, 0.001)
nBCC	0.319	(0.144, 0.494)
iBCC/mnBCC	0.185	(-0.02, 0.389)
No BCC	0.318	(0.127, 0.509)

Deep-learning algorithm: Most nBCC regions were segmented (Fig. 9, Table 4). The integrated segmentation and classification model showed better performance than the segmentation-only model. The artifact of the FOV boundary was significantly reduced when comparing the results of focal loss and cross-entropy loss. The false positives on nBCC are significantly reduced, and the mIOU increased to 60.3%±10.1%. The sensitivity and specificity reach 93.5%±2.2% and 81.2% ±9.2%, respectively.

Table 4
Summary of the nBCC segmentation and detection results.

Nodular BCC		Segmentation model only		Segmentation + classification models	
		Cross entropy loss	Focal loss	Hard vote	Soft vote
Segmentation	Mean IoU	46.4%±12.7%	51.6%±11.9%	60.1%±10.6%	*60.3%±10.1%
Detection	Accuracy	86.2%±6.2%	87.1%±7.3%	*87.8%±6.8%	87.6%±5.9%
	Sensitivity	94.3%±2.9%	93.2%±3.1%	*93.5%±2.2%	93.2%±2.1%
	Specificity	79.5%±11.4%	79.8%±10.7%	81.1%±9.9%	*81.2%±9.2%
	PPV	78.7%±12.5%	79.6%±13.2%	80.4%±10.8%	*80.5%±11.3%
	NPV	93.4%±2.6%	93.1%±2.1%	93.2%±2.3%	*93.3%±1.6%

Abbreviations: BCC: Basal cell carcinoma. *Represent best results

Discussion

In this manuscript, we described, for the first time, cellular features of normal skin and NMSCs including BCC, and a benign lesion with a novel high-resolution FF-OCT device in fresh ex vivo tissues. Through a blinded analysis, we demonstrated the potential utility of this device for identifying and classifying neoplastic keratinocytic lesions. The FF-OCT had high sensitivity in detecting all the tumors but had a low-moderate specificity.

Amongst all tumor types, nBCC had the highest sensitivity for tumor detection, however, had a moderate specificity. False-positive results were due to the inability to distinguish tumor nodules from sebaceous glands. However, sebaceous glands exhibit bright punctate dots and have sparse surrounding collagen that can aid in differentiating their identification. The deep learning algorithms employed could largely segment nBCC regions. However, there were still some false positives on nBCC segmentation, which might be due to the similar OCT appearance between nBCC and sebaceous glands. On the contrary, SCC and sBCC had low sensitivity but very high specificity. The low sensitivity could be a result of incomplete visualization of the epidermis, which hindered the detection of these tumors originating from the epidermis. Incomplete visualization of the epidermis was caused by the use of tangentially excised Mohs specimens and resultant tissue flattening issues encountered during imaging. We believe such an issue can be improved with a vertically excised specimen. In the future, it may also be possible to resolve the flattening issue by using the newly described digital tissue flattening[26], which can use then expand the application of this device to evaluate Mohs surgical margins. Similarly, iBCCs and mnBCCs had a low sensitivity. This could possibly be due to the difficulty of identifying small strands or foci of these tumors among the bright and dense collagenous background.

The inter-rater reliability (Kohen's kappa, **Table 3**) values of the two OCT experts were below 0.4. This could be related to the inability to differentiate BCC tumor nests from normal sebaceous glands or follicular epithelium by the grayscale imaging, especially for small BCC strands or nests. Ex vivo confocal microscope can create digitally colored purple and pink images that simulates H&E-stained tissue sections.

The major limitation of this study was a small sample of tumors. Another limitation is the gray-scale nature of images that requires interpretation by experts in this field. Thus, future studies are warranted using a large sample size (including benign lesions) and performing a multi-reader diagnostic accuracy study. Furthermore, deep learning algorithms can be integrated to convert grayscale images into digitally colored purple and pink images[27], similar to the images created by an ex vivo confocal microscope. This would improve visualization of the OCT images and reduce the learning curve . Moreover, AI can aid in the automated detection of tumors, leading to its wider adoption[20,28].

Based on our pilot study, we envision FF-OCT as an alternative for time-consuming and tedious histopathology to enable a rapid assessment of the tumor margins in the surgical excision samples, potentially reducing their recurrence rate. At least, FF-OCT may offer a role in initial specimen screening for the margin status in the operation room to facilitate completeness of tumor removal before conventional histological confirmation. It can also be combined with the in-vivo imaging techniques such as optical coherence tomography and confocal microscopy that has limited penetration depth and often cannot used to evaluate deeper surgical margins. Additionally, FF-OCT can analyze small biopsies at the bedside before they are submerged in formalin for further processing. If indicated, all or part of the specimen can be preserved for molecular analysis as the tissue is neither processed nor sectioned. Lastly, since the FF-OCT images are digitally stored they can be read and analyzed remotely by a specialist, as a telehealth tool[29], for evaluation of ex vivo tissue, especially beneficial for rural or underserved areas. Although different ex vivo imaging technologies exists, knowledge of this novel device is essential to the consumers so they can tailor their needs based on the device cost and capability. Ultimately, ex-vivo OCT may not necessary replace the current rapid pathology process but may help to fill the gap in the under-served community or rural area where an extensive lab set-up and trained technicians may not be readily available.

Declarations

Conflicts of Interest: Manu Jain is a consultant for Enspectra Health Inc. (not relevant for this article). Chih-Shan Jason Chen is the Principal Investigator of Apollo Medical Optics, Ltd. sponsored research projects. Sheng-Lung Huang was a co-founder and the Chief Science Officer of Apollo Medical Optics, Ltd.

IRB approval status: Reviewed and approved by Western IRB; approval #08-006

Clinicaltrials.gov (or equivalent): None

References

1. Rogers HW, Weinstock MA, Feldman SR, Coldiron BM. Incidence Estimate of Nonmelanoma Skin Cancer (Keratinocyte Carcinomas) in the U.S. Population, 2012. *JAMA dermatology*. Oct 2015;151(10):1081-6. doi:10.1001/jamadermatol.2015.1187

2. Fahradyan A, Howell AC, Wolfswinkel EM, Tsuha M, Sheth P, Wong AK. Updates on the Management of Non-Melanoma Skin Cancer (NMSC). *Healthcare (Basel)*. Nov 1 2017;5(4)doi:10.3390/healthcare5040082

3. Mosterd K, Krekels GA, Nieman FH, et al. Surgical excision versus Mohs' micrographic surgery for primary and recurrent basal-cell carcinoma of the face: a prospective randomised controlled trial with 5-years' follow-up. Lancet Oncol. Dec 2008;9(12):1149–56. doi:10.1016/S1470-2045(08)70260-2

4. Taxy JB. Frozen section and the surgical pathologist: a point of view. Archives of pathology & laboratory medicine. Jul 2009;133(7):1135–8. doi:10.1043/1543-2165-133.7.1135 5858/133.7.1135

5. Jain M, Narula N, Salamoon B, et al. Full-field optical coherence tomography for the analysis of fresh unstained human lobectomy specimens. J Pathol Inform. 2013;4:26. doi:10.4103/2153-3539.119004

6. Jerjes W, Hamdoon Z, Al-Rawi N, Hopper C. Optical coherence tomography in the assessment of cutaneous cancer margins of the face: An immediate ex vivo study. Photodiagnosis and photodynamic therapy. Mar 2020;29:101616. doi:10.1016/j.pdpdt.2019.101616

7. Jain M, Robinson BD, Salamoon B, Thouvenin O, Boccara C, Mukherjee S. Rapid evaluation of fresh ex vivo kidney tissue with full-field optical coherence tomography. J Pathol Inform. 2015;6:53. doi:10.4103/2153-3539.166014

8. Levine A, Wang K, Markowitz O. Optical Coherence Tomography in the Diagnosis of Skin Cancer. Dermatologic clinics. Oct 2017;35(4):465–488. doi:10.1016/j.det.2017.06.008

9. Cunha D, Richardson T, Sheth N, Orchard G, Coleman A, Mallipeddi R. Comparison of ex vivo optical coherence tomography with conventional frozen-section histology for visualizing basal cell carcinoma during Mohs micrographic surgery. The British journal of dermatology. Sep 2011;165(3):576–80. doi:10.1111/j.1365-2133.2011.10461.x

10. Jain M, Rajadhyaksha M, Nehal K. Implementation of fluorescence confocal mosaicking microscopy by "early adopter" Mohs surgeons and dermatologists: recent progress. J Biomed Opt. Feb 1 2017;22(2):24002. doi:10.1117/1.JBO.22.2.024002

11. Krishnamurthy S, Brown JQ, Iftimia N, Levenson RM, Rajadhyaksha M. Ex Vivo Microscopy: A Promising Next-Generation Digital Microscopy Tool for Surgical Pathology Practice. *Archives of pathology & laboratory medicine*. Sep 2019;143(9):1058–1068. doi:10.5858/arpa.2019-0058-RA

12. Welzel J. Optical coherence tomography in dermatology: a review. *Skin research and technology: official journal of International Society for Bioengineering and the Skin*. Feb 2001;7(1):1–9. doi:10.1034/j.1600-0846.2001.007001001.x

13. Jung W, Boppart SA. Optical coherence tomography for rapid tissue screening and directed histological sectioning. Stud Health Technol Inform. 2013;185:109–28.

14. Wang YJ, Chang WC, Wang JY, Wu YH. Ex vivo full-field cellular-resolution optical coherence tomography of basal cell carcinomas: A pilot study of quality and feasibility of images and diagnostic accuracy in subtypes. Skin research and technology: official journal of International Society for Bioengineering and the Skin. Mar 2020;26(2):308–316. doi:10.1111/srt.12801

15. Tsai CC, Chang CK, Hsu KY, et al. Full-depth epidermis tomography using a Mirau-based full-field optical coherence tomography. Biomed Opt Express. Sep 1 2014;5(9):3001–10. doi:10.1364/BOE.5.003001

16. Ho TS, Tsai MR, Lu CW, Chang HS, Huang SL. Mirau-type full-field optical coherence tomography with switchable partially spatially coherent illumination modes. Biomed Opt Express. May 1 2021;12(5):2670–2683. doi:10.1364/BOE.422622

17. Ho CJ, Calderon-Delgado M, Lin MY, Tjiu JW, Huang SL, Chen HH. Classification of squamous cell carcinoma from FF-OCT images: Data selection and progressive model construction. Computerized medical imaging and graphics: the official journal of the Computerized Medical Imaging Society. Oct 2021;93:101992. doi:10.1016/j.compmedimag.2021.101992

18. Chou HY, Huang SL, Tjiu JW, Chen HH. Dermal epidermal junction detection for full-field optical coherence tomography data of human skin by deep learning. Computerized medical imaging and graphics: the official journal of the Computerized Medical Imaging Society. Jan 2021;87:101833. doi:10.1016/j.compmedimag.2020.101833

19. Litjens G, Kooi T, Bejnordi BE, et al. A survey on deep learning in medical image analysis. Med Image Anal. Dec 2017;42:60–88. doi:10.1016/j.media.2017.07.005

20. Sendin-Martin M, Lara-Caro M, Harris U, et al. Classification of Basal Cell Carcinoma in Ex Vivo Confocal Microscopy Images from Freshly Excised Tissues Using a Deep Learning Algorithm. J Invest Dermatol. May 2022;142(5):1291–1299 e2. doi:10.1016/j.jid.2021.09.029

21. Zeng Z, Xie W, Zhang Y, Y. L. RIC-Unet: An improved neural network based on Unet for nuclei segmentation in histology images. IEEE Access. 2019;7:21420–21428.

22. Xie L, Qi J, Pan L, S. W. Integrating deep convolutional neural networks with marker-controlled watershed for overlapping nuclei segmentation in histopathology images.. Neurocomputing. 2020;376:166–179.

23. Pfister M, Schutzenberger K, Pfeiffenberger U, et al. Automated segmentation of dermal fillers in OCT images of mice using convolutional neural networks. Biomed Opt Express. Mar 1 2019;10(3):1315–1328. doi:10.1364/BOE.10.001315

24. Ronneberger O, Fischer P, Brox T. U-Net: Convolutional Networks for Biomedical Image Segmentation. Lect Notes Comput Sc. 2015;9351:234–241. doi:10.1007/978-3-319-24574-4_28

25. Lin TY, Goyal P, Girshick R, He KM, Dollar P. Focal Loss for Dense Object Detection. Ieee T Pattern Anal. Feb 2020;42(2):318–327. doi:10.1109/Tpami.2018.2858826

26. Sendin-Martin M, Kose K, Harris U, et al. Complete visualization of epidermal margin during ex vivo confocal microscopy of excised tissue with 3-dimensional mosaicking and intensity projection. Journal of the American Academy of Dermatology. Jan 2022;86(1):e13-e14. doi:10.1016/j.jaad.2020.05.044

27. Sheng-Ting Tsai, Chih-Hao Liu, Chin-Cheng Chan, Yi-Hsin Li, Sheng-Lung Huang, Chen HH. H&E-like staining of OCT images of human skin via generative adversarial network. Appl Phys Lett 2022;121:134102.

28. Combalia M, Garcia S, Malvehy J, et al. Deep learning automated pathology in ex vivo microscopy. Biomed Opt Express. Jun 1 2021;12(6):3103–3116. doi:10.1364/BOE.422168

29. Rubinstein G, Garfinkel J, Jain M. Live, remote control of an in vivo reflectance confocal microscope for diagnosis of basal cell carcinoma at the bedside of a patient 2500 miles away: A novel tele-reflectance confocal microscope approach. Journal of the American Academy of Dermatology. Aug 2019;81(2):e41-e42. doi:10.1016/j.jaad.2019.02.016

Figures

Figure 1

The U-Net configuration with the designed image sizes (at the sides of the green rectangles) and convolution core numbers (on or below the green rectangles).

Figure 2

Images of normal layers of the skin. (A) FF-OCT image showing grayish epidermal lining (pink arrow), dermis (green asterisk), and underlying subcutis (pink asterisk). (B) A stratified layer of the epidermis (pink arrow) shows multiple round to oval dark nuclei surrounded by bright (grayish) cytoplasm. The underlying dermis appears grayish (green asterisk). (C) Adipocytes of the subcutis appear as dark polygonal structures separated by thin white septa (pink asterisk). (D-F) Corresponding histopathology section stained with Toluidine blue. Magnifications: (A) = 5.2 mm x 5.2 mm; (B, C) = 300 x 150 mm; (D)= 10x; (E, F) = 40x .
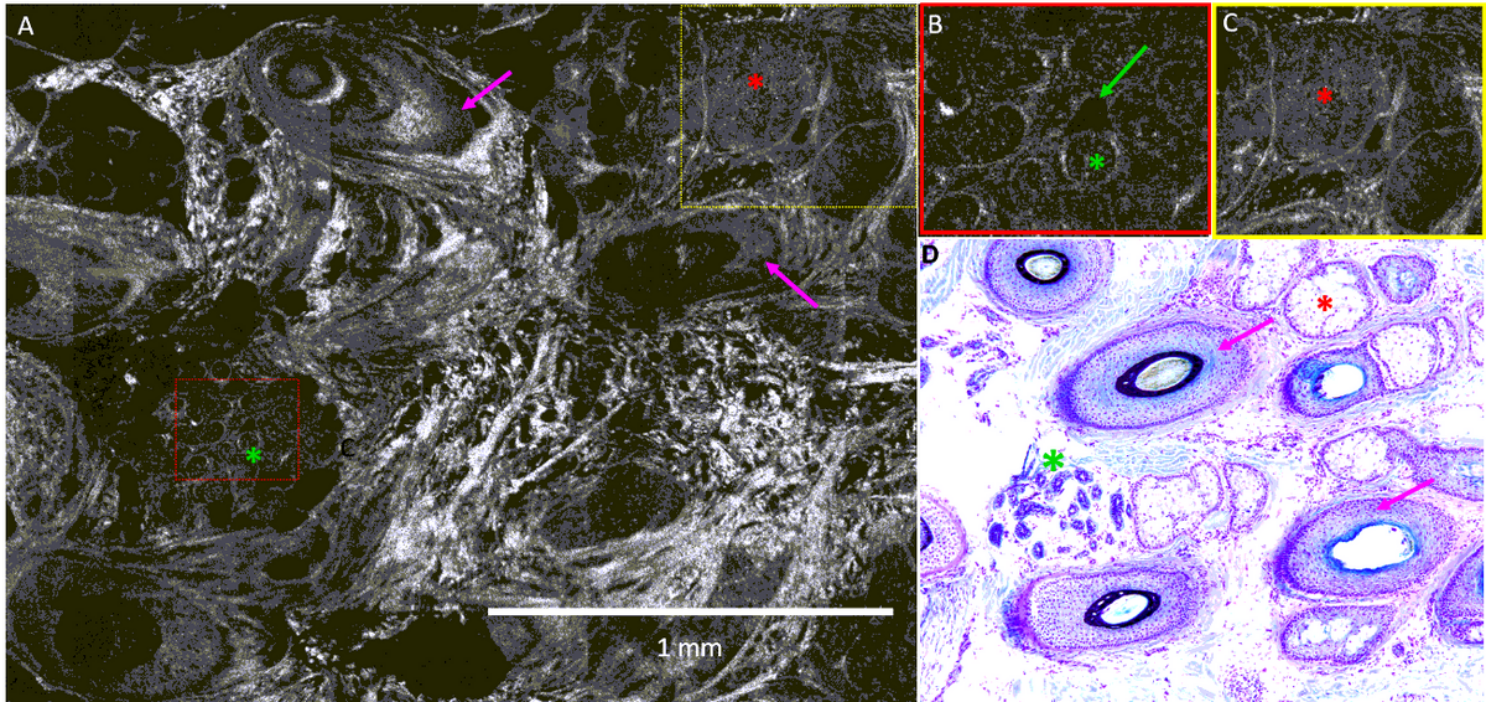
Figure 3

Images of normal adnexal structures of the skin. (A) FF-OCT image showing hair follicles (pink arrows) in longitudinal section, eccrine unit (green asterisk), and sebaceous lobules (red asterisk). (B) Eccrine glands appear as tightly packed clusters of round to ovoid structures with some bright particles. A central duct is seen as a dark oval structure (green arrow) lined by a grayish lining. (C) Sebaceous gland lobules appear round to oval darkish (hypo-reflective) structures with bright punctate particles. (D) Corresponding histopathology section stained with Toluidine blue. Magnifications: (A): Scale bar is 1 mm; (B) = 300 x 240 mm; (C)= 600 x 500 mm; (D)= 10x.
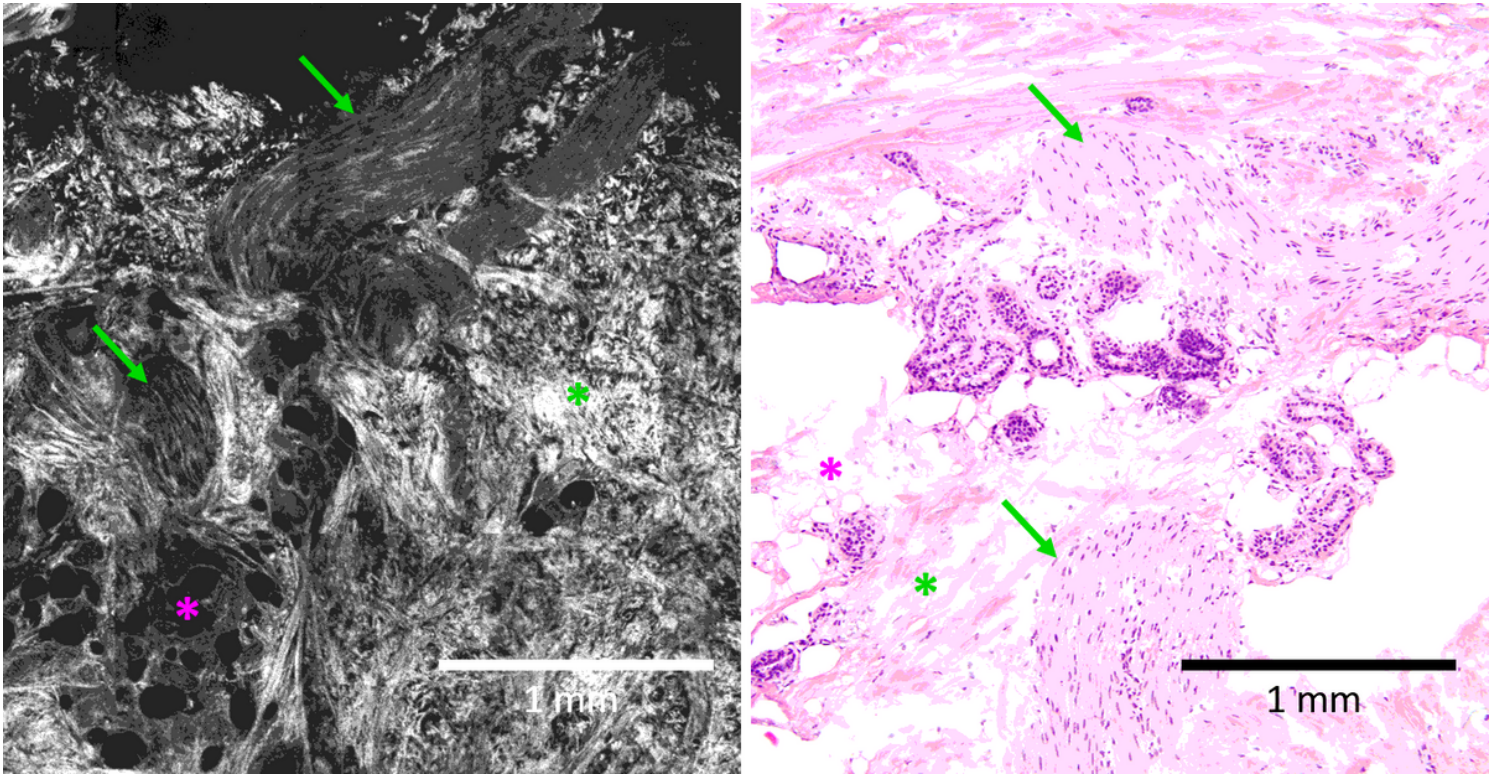
Figure 4

Images of the smooth muscle of the skin. (A) FF-OCT image showing grayish smooth muscle bundles (green arrows) in longitudinal section with cigar-shaped dark elongated nuclei within and the surrounding fibrofatty tissue (collagen: green asterisk; adipocytes red asterisk). (B) Corresponding histopathology section stained with H&E. Magnifications: Scale bar: 1 mm; (B) = 10x.
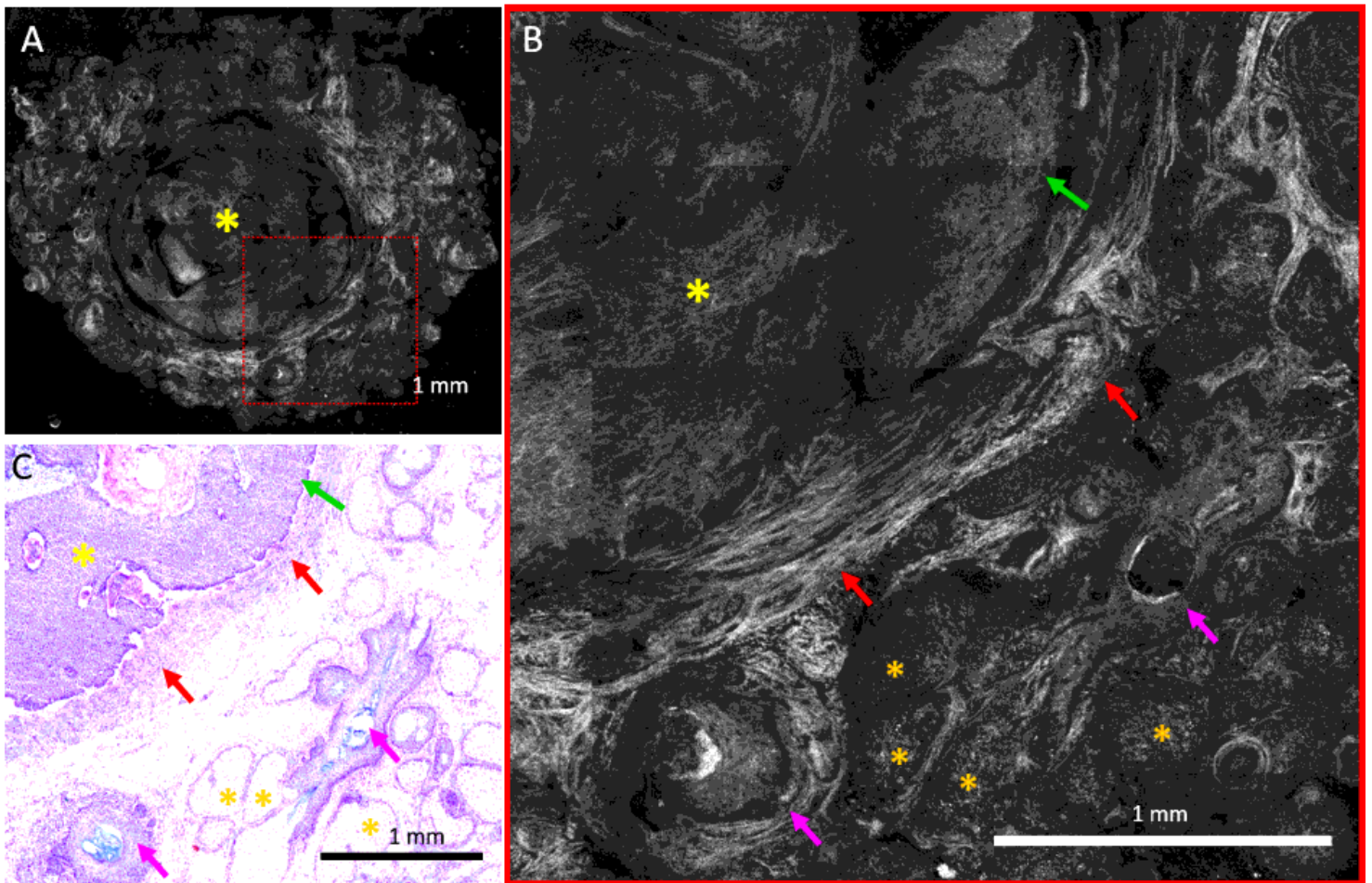
Figure 5

Features of a nodular basal cell carcinoma (BCC) as compared to the normal adnexal structures: A) FFOCT image shows a big BCC nodule (yellow asterisk) surrounded by normal skin structures. B) Zoomed-in area from the red box in the image (A) shows cellular features of BCC with nuclear atypia, peripheral palisading (green arrow), and clefting (yellow arrow). The nodule is surrounded by a thick bright band of collagen (red arrows). Sebaceous glands (orange asterisks) have a lobulated appearance with bright punctate structures. The hair follicles (pink arrows) appear round to oval with a central lumen and epidermal lining. C) Corresponding H&E-stained histopathology image. Scale bars = 1 mm.
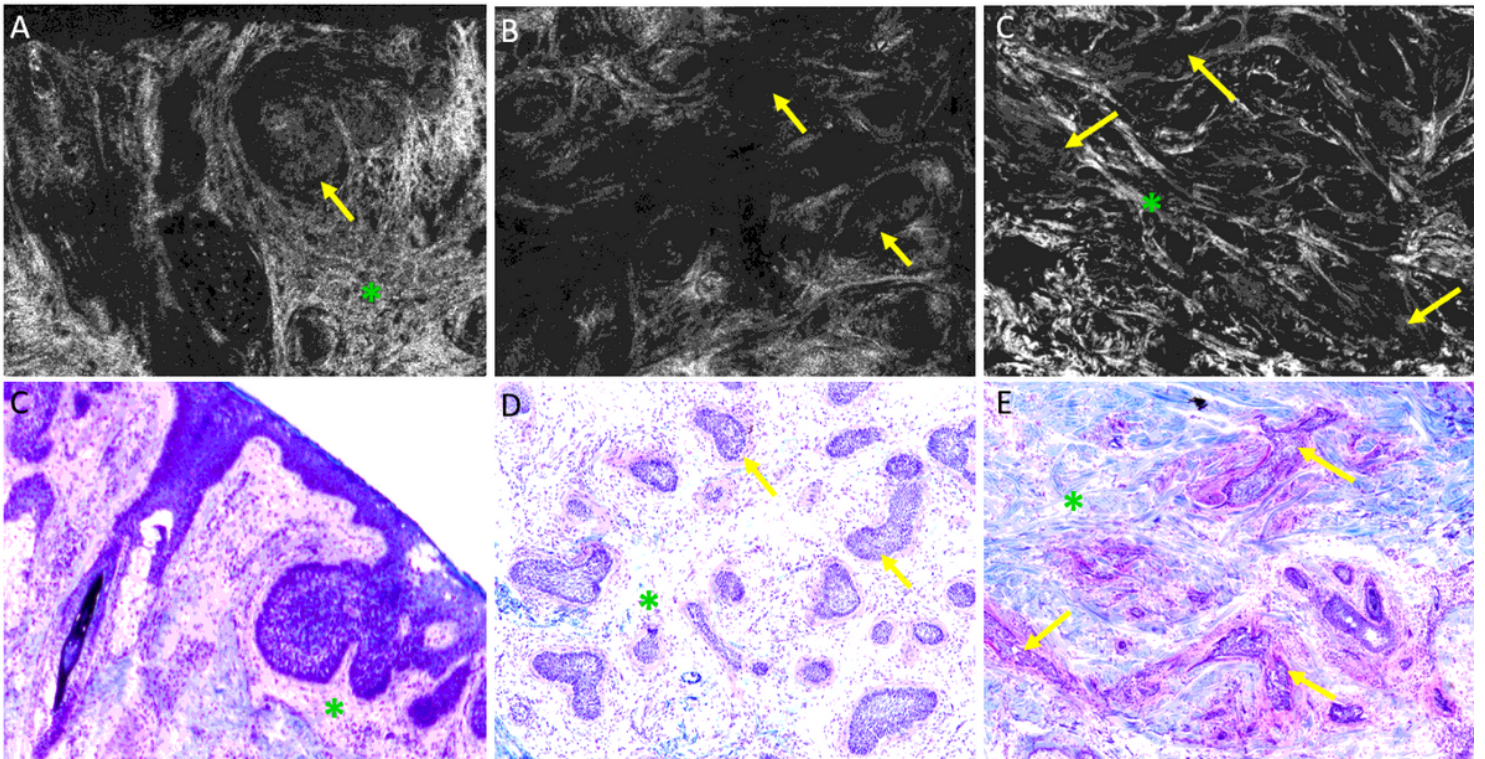
Figure 6

Images of basal cell carcinoma (BCC) subtypes. FF-OCT images: (A) superficial BCC with grayish tumor nodules (yellow arrow). Epidermal attachment is not visible due to the lack of epidermis caused by inadequate tissue flattening. (B) micronodular BCC with small grayish tumor nodules, and (C) infiltrative BCC with grayish tumor strands (yellow arrows). BCC nodules are surrounded by a collagenous matrix. (D-F) Corresponding histopathology sections with Toluidine blue. Magnifications: (A-C) = 2 x 1.5 mm; (D-F) = 10x.
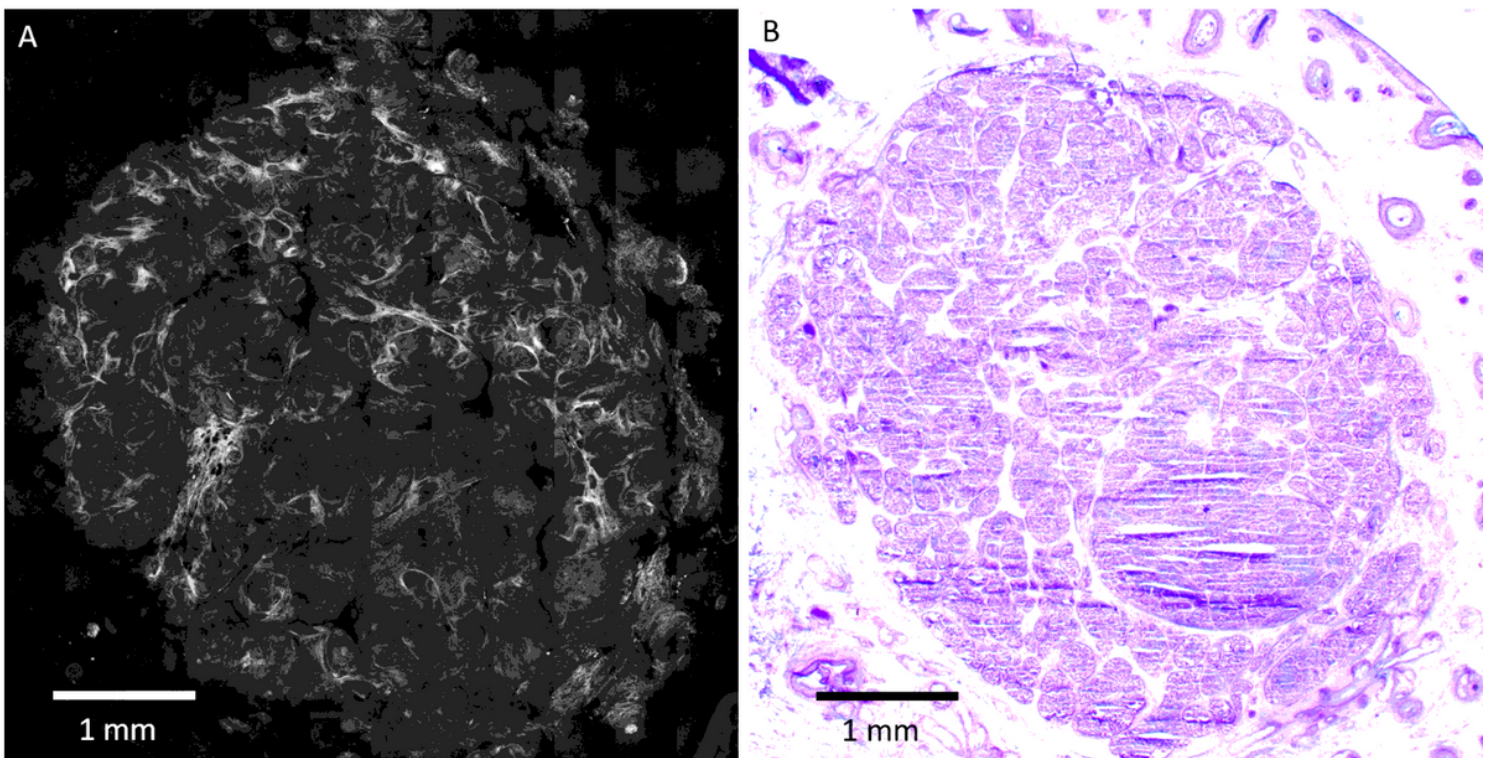

Figure 8

Image of a cylindroma. A) FF-OCT image shows a well-circumscribed large multi-lobated grayish structure within the dermis. (B) Corresponding histopathology section stained with Toluidine blue. Scale bar: 1 mm.
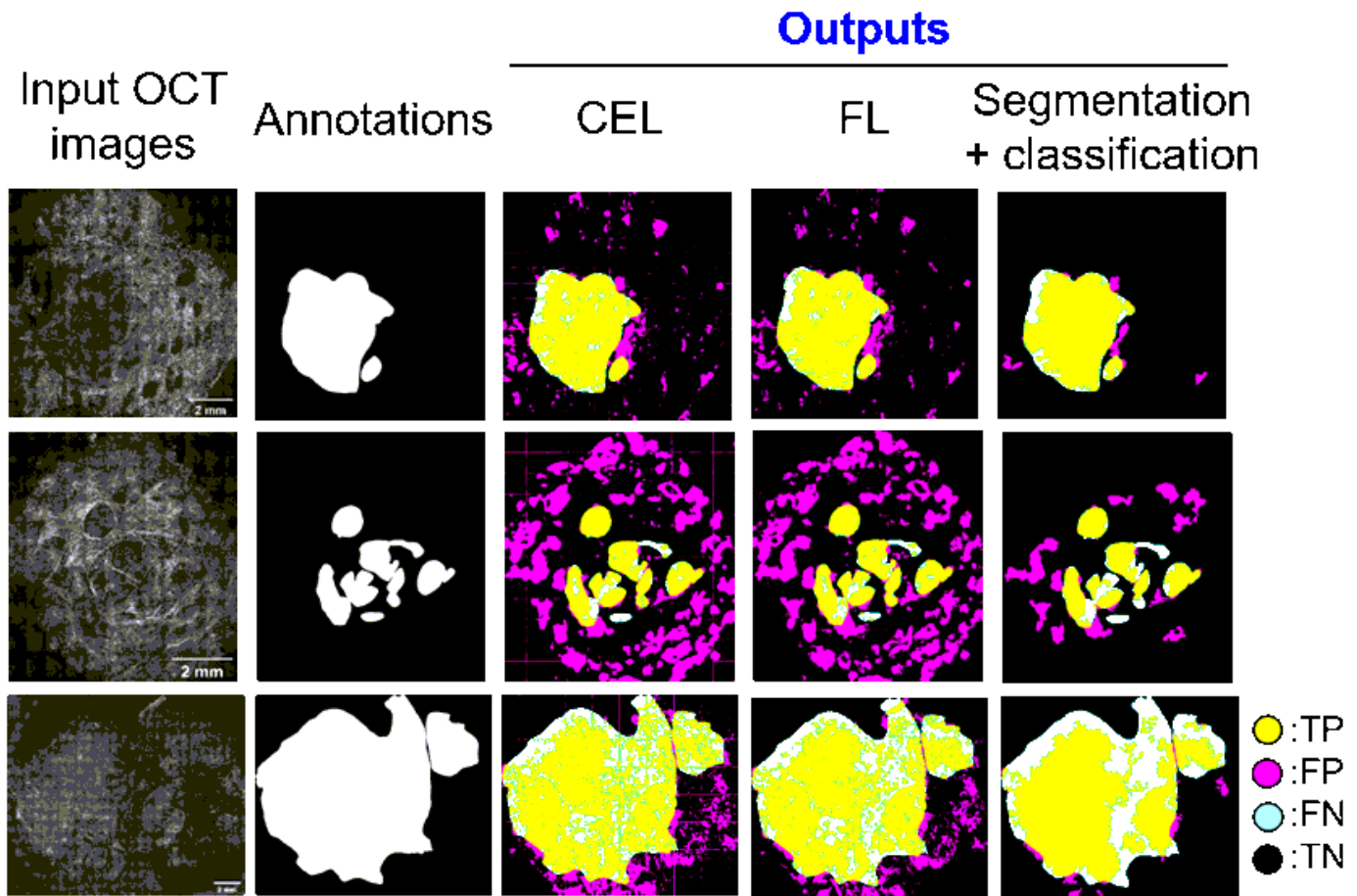

Figure 9

The image segmentation results of 3 patients. CEL: cross-entropy loss, FL: focal loss. The 49 white color in the annotation column represents the nBCC regions. The scale bars are all 2 mm. The 50 color-coding of yellow, pink, cyan, and black represent true positive, false positive, false negative, and 51 true negative, respectively.